Pure Appl. Geophys. 181 (2024), 2973–2990

https://doi.org/10.1007/s00024-024-03554-5

Pure and Applied Geophysics

Crustal Structure and its Control on Gold Mineralization in Wulong Goldfield, Liaodong Peninsula of China: Constraints from Ambient Noise Tomography with a Short-Period Dense Array

Tingwei Yang,[1,5] Tao Xu,[1,4] Yinshuang Ai,[2,4,5] Qingdong Zeng,[1,4,5] Jinhui Yang,[3,4] Laicheng Miao,[1,4] Fan Zheng,[3,5] and Nanqiao Du[6]

Abstract—During the destruction of the North China Craton in the Mesozoic era, a significant gold mineralization event occurred, leading to the formation of the world-renowned Jiaodong Gold Province. The Liaodong and Jiaodong regions have similar tectonic backgrounds and geological evolution histories. However, the confirmed gold resources in the Liaodong region are only one-tenth of those in Jiaodong. To reveal the controlling factors behind the differences in mineralization between these two regions and explore the deep mineralization prospects in the Liaodong region, we conducted a short-period and high-density array (WSP array) in the Wulong Gold Concentrated Area, the largest goldfield in the Liaodong region. Using data recorded by 334 SmartSolo seismometers for one month, we applied ambient noise tomography to obtain the S-wave velocity structure of the crust down to a depth of 3.5 km beneath the Wulong goldfield. The velocity structure revealed the presence of two sets of low-velocity anomalies trending NNE and NW, respectively, in the shallow crust (shallower than 1.5 km) of the Wulong goldfield, while two high-velocity anomalies were identified at deeper depths (1.5–3.5 km). By combining these findings with the geological characteristics of the Wulong goldfield, it was discovered that the high-velocity anomaly (II) corresponds to the Sanguliu granitic body exposed at the surface, while the high-velocity anomaly (I) could be a concealed intrusive body. The shallow low-velocity anomalies are the result of hydrothermal alteration caused by mineralizing fluids along the NNE- and NW-trending faults. The intersection of these two sets of faults, where the low-velocity anomalies exist, represents the center of the hydrothermal activities. Based on these observations, it is proposed that the area between the Sanguliu granitic body and the concealed intrusive body in the northwest has favorable metallogenic conditions. The intersections of the NNE- and NW-trending faults show the high potential for forming large to super-large altered rock-type gold deposits.

Keywords: Wulong goldfield, short-period dense array, ambient noise tomography, crustal velocity structure.

Tingwei Yang, Tao Xu, Fan Zheng, YinShuang Ai, and NanQiao Du conducted the data analysis, method development, and result description, and they initially drafted the manuscript. QingDong Zeng, JinHui Yang, and LaiCheng Miao contributed to the interpretation. All authors participated in reviewing and approving the final version of the manuscript before submission.

[1] Key Laboratory of Mineral Resources, Institute of Geology and Geophysics, Chinese Academy of Sciences, Beijing 100029, China. E-mail: twyang@mail.iggcas.ac.cn; xutao@mail.iggcas.ac.cn; zengqingdong@mail.igcas.ac.cn; miaolc@mail.igcas.ac.cn

[2] Key Laboratory of Earth and Planetary Physics, Institute of Geology and Geophysics, Chinese Academy of Sciences, Beijing 100029, China. E-mail: ysai@mail.iggcas.ac.cn

[3] State Key Laboratory of Lithospheric Evolution, Institute of Geology and Geophysics, Chinese Academy of Sciences, Beijing 100029, China. E-mail: jinhui@mail.igcas.ac.cn; zhengfan@aircas.ac.cn

[4] Innovation Academy for Earth Science, Chinese Academy of Sciences, Beijing 100029, China.

[5] University of Chinese Academy of Sciences, Beijing 100049, China.

[6] Department of Earth Science, University of Toronto, Toronto, Canada. E-mail: nanqiao.du@mail.utoronto.ca

1. Introduction

The North China Craton (NCC) is the largest and oldest continental block in China, with basement rocks dating back to 3.8 Ga (Liu et al., 1992). The northern side of the NCC is bordered by the Paleozoic Central Asian Orogenic Belt, while the southern side is bounded by the Paleozoic to Early Mesozoic Qinling–Dabie–Sulu Orogenic Belt (Zhu et al., 2024). The eastern side is characterized by the Mesozoic to Cenozoic Circum-Pacific Orogenic Belt (Miao et al., 2005; Dong et al., 2022; Yang et al., 2024). Along these tectonic belts, particularly in the eastern part of the NCC, numerous large-scale gold deposits have been developed. Previous studies have indicated that these gold deposits formed in tectonic settings transitioning from compression to extension or during the large-scale lithospheric thinning or decratonization in the late Mesozoic in the eastern

NCC (Zhai et al., 2002; Zhu et al., 2015; Li et al., 2020; Zhu et al., 2021). However, the spatial distribution and mineralization density of gold deposits in the eastern NCC, including the Jiaodong and Liaodong Peninsulas, exhibit significant heterogeneity (Ma et al., 2022; Xu et al., 2023). For instance, both the Jiaodong and Liaodong Peninsulas are located on the northwest side of the Dabie-Sulu suture zone and share similar or identical tectonic–magmatic histories, mineralization ages, and geological characteristics of the ore deposits (Deng et al., 2020; Li et al., 2015; Zeng et al., 2019). However, the Jiaodong Peninsula currently has confirmed gold reserves of about 5000 tons, making it the largest gold production base in China, while the confirmed reserves in the Liaodong Peninsula are only around 500 tons (Zeng et al., 2019). The key factors controlling this regional heterogeneity in mineralization are not yet understood. Some researchers suggest that the difference in exploration depth may be one of the crucial reasons for the significant disparity in gold reserves between Jiaodong and Liaodong. This is because the exploration depth in Jiaodong has reached depths of up to 5000 m, while the deepest borehole in the Liaodong region is only around 1000 m (Yu et al., 2018, 2020; Zeng et al., 2019). If this understanding is correct, the deep part of the Liaodong Peninsula will have significant potential for mineral exploration (Xie et al., 2021; Zheng et al., 2024).

Geophysical exploration is one of the effective methods for revealing the deep mineral exploration potential. Currently, geophysical surveys, especially those for individual deposits in Liaodong, are still relatively rare. Xu et al. (2018) obtained a detailed three-dimensional P-wave velocity model of the entire North China Craton using the finite-frequency body wave tomography method, and Fan et al. (2021) established a high-resolution three-dimensional crust-mantle S-wave velocity model for Northeast China based on dense seismic array combined with ambient noise and seismic double-plane wave tomography techniques. Both studies involved in the Liaodong region and provided valuable insights into the lithospheric structure and mantle dynamics in the Liaodong region. However, there is still a lack of detailed knowledge about the fine structures beneath key goldfields in Liaodong. Recently, Zheng et al. (2022) used a direct inversion method of Rayleigh wave group velocity dispersion to study the shallow fine structures in the Wulong goldfield in Liaodong and discovered a concealed NW-trending fault beneath the Wulong goldfield. However, the imaging depth of this result is shallow, only providing detailed structures down to a depth of 1.5 km. Clearly, this result lacks constraints on the deeper structures in the Wulong goldfield.

To address this, we have utilized the ambient noise data obtained from the short-period, high-density seismic array (WSP) in the Wulong goldfield of Liaodong. By employing a joint inversion method based on phase velocity and group velocity, we aim to obtain the S-wave velocity structure beneath the Wulong goldfield to the depth of 3.5 km, providing new constraints for understanding and evaluating the deep mineralization potential in the Wulong goldfield.

2. *Geological Setting*

The basement of the Liaodong Peninsula is composed of the Archean Anshan Group and the Paleoproterozoic Liaohe Group metamorphic rocks. The Anshan Group is mainly distributed in the northern and southern parts of the Liaodong Peninsula and consists primarily of tonalite-trondhjemite-granodiorite (TTG) and metamorphic supracrustal rocks (Feng et al., 2020; Gu et al., 2018; Liu et al., 1992). The Archean Anshan Group hosts the largest banded iron formation deposits in China. The Paleoproterozoic Liaohe Group is located between the northern and southern parts of the Liaodong Peninsula and is considered to be a sedimentary sequence formed in the Liaohe Rift basin. It is divided, from bottom to top, into the Langzishan, Lieryu, Gaojiayu, Dashiqiao, and Gaixian Formations (Luo et al., 2004; Zeng et al., 2019). The Langzishan Formation consists mainly of biotite-chlorite schist and garnet-staurolite-mica schist. The Lieryu Formation is known as the “boron-bearing stratigraphic unit” and mainly comprises magnetite-bearing and tourmaline, including lenses of amphibolite and deposits of boron and magnetite. The Gaojiayu Formation is dominated by graphite-bearing schist, biotite schist, and marble, and it hosts the primary lead–zinc deposits in the Liaodong Peninsula. The Dashiqiao Formation consists of thick-bedded dolomite and interlayers of mica schist and carbonaceous slate. It is the host unit for magnesite, talc, and lead–zinc deposits in the Liaodong region. The Gaixian Formation mainly comprises quartzite, zeolite-mica schist, chert-staurolite-mica schist, and minor marble, and it serves as an important unit hosting gold deposit (Duan et al., 2014; Li et al., 2015). The Liaohe Group underwent greenstone-amphibolite facies metamorphism around 1.85 Ga ago, which is contemporaneous with the cratonization of the NCC (Li et al., 2015).

The early Precambrian basement of Liaodong is unconformably covered by the Neoproterozoic Yongning Group and by shallow marine carbonate rocks and mudstones of the Cambrian-Ordovician. These units were in turn overlain by Carboniferous-Permian coal-bearing sedimentary sequences characterized by marine and terrestrial intercalations. The Neoproterozoic Yongning Group (also known as "Yongning Sandstone"; Geological Bureau of Liaoning Province, 1989) consists of a series of turbidite deposits (Yu et al., 2020). Silurian-Devonian and Triassic strata are missing in the entire Liaodong area.

According to the spatial distribution characteristics of gold deposits, the Liaodong Peninsula can be roughly divided into three major gold concentrated districts: Qingchengzi, Maoling, and Wulong (Fig. 1b; Zeng et al., 2019). The Qingchengzi gold concentrated district is located in the northern part of the Liaodong Peninsula, and it primarily hosts gold deposits such as Baiyun, Xiaotongjiapuzi, and Linjiasandaogou (Liu et al., 2020). The Maoling district consists of the Maoling large-scale gold deposit and other small-scale deposits and occurrences (Yu et al., 2020; Zhang et al., 2017). The Wulong goldfield (WLGF) includes two large-scale gold deposits, Wulong and Sidaogou, as well as several small-scale gold deposits and occurrences (Feng et al., 2019; Yu et al., 2020). Among these three gold concentrated districts, the Wulong one is the most economically significant in terms of gold production and reserve, owing to it containing the Wulong gold deposit, the largest one in the Liaodong region, with a gold reserve exceeding 80 tons (Yu et al., 2020).

The exposed strata in the WLGF mainly consist of the Paleoproterozoic Liaohe Group and the Neoproterozoic Yongning Group (Zeng et al., 2019). Within the WLGF, the Liaohe Group is represented by the Lieryu Formation and Gaixian Formation, which are distributed on the southwestern and southeastern margins of the goldfield. The Yongning Group is only found near the Sidaogou gold deposit (Fig. 1c) in the southeastern part of the Yellow River Delta (Duan et al., 2014; Yu et al., 2020). The WLGF is intruded by a large number of Mesozoic granitic intrusions, with the Wulong and Sanguliu intrusive bodies being the most prominent. The Wulong intrusive body, emplaced in the Late Jurassic (with a zircon U–Pb age of approximately 160 Ma) (Wang et al., 2019), mainly consists of biotite-bearing diorite and biotite-bearing monzogranite, representing the largest intrusion in the mining district (Fig. 1c). The Sanguliu intrusive body is smaller in scale and composed of monzogranite and granodiorite, with the monzogranite occurring in the central part of the intrusion and the granodiorite (with minor quartz diorite) distributed at the edges of the intrusion. Zircon dating indicates that the monzogranite in the central part and the granodiorite at the edges were simultaneously formed in the Early Cretaceous (131–120 Ma) (Wang et al., 2020). In addition, the Wulongbei intrusion is developed in the northwestern part of the goldfield, primarily composed of monzogranite, formed in the Early Cretaceous at around 135 Ma (Wu et al., 2005). In the WLGF, particularly within the Wulong mining area, various types of dikes develop, including diorite (fenite), granodiorite (porphyry), granite porphyry, and lamprophyre dike. These dikes have a close temporal and spatial relationship with gold-bearing quartz veins.

The WLGF is characterized by the development of faults, with the NNE-trending faults being the most prominent (Yu et al., 2018; Zhang et al., 2020; Fig. 1c). These NNE-trending faults have a strike of approximately 25–30°, dipping to the northwest at angles ranging from 50° to 80°. They are considered secondary faults of the Yalujiang Fault (Zhang et al., 2019). The Yalujiang Fault is a regional sinistral strike-slip fault that trends northeast and extends generally along Yalujiang, the border river between China and North Korea, which forms the southeastern

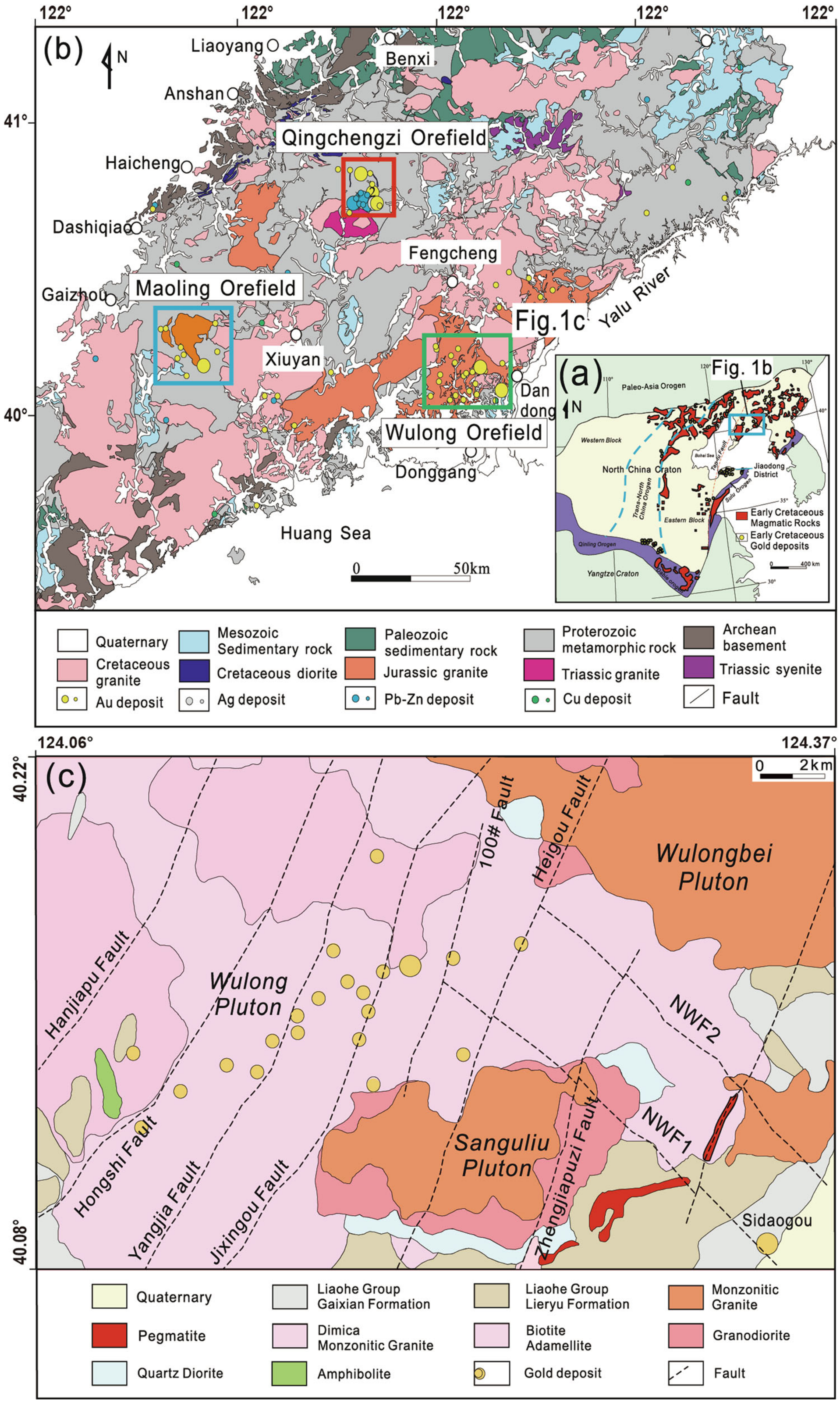

122°
122°
122°
122°
122°
41°
40°
(b)
N
Liaoyang
Benxi
Anshan
Qingchengzi Orefield
Haicheng
Dashiqiao
Fengcheng
Gaizhou
Maoling Orefield
Yalu River
Fig.1c
Xiuyan
Dan dong
Wulong Orefield
Donggang
Huang Sea
0 50km
(a)
Fig. 1b
Paleo-Asia Orogen
Western Block
North China Craton
Jiaodong District
Eastern Block
Qinling Orogen
Yangtze Craton
Early Cretaceous Magmatic Rocks
Early Cretaceous Gold deposits
Quaternary
Mesozoic Sedimentary rock
Paleozoic sedimentary rock
Proterozoic metamorphic rock
Archean basement
Cretaceous granite
Cretaceous diorite
Jurassic granite
Triassic granite
Triassic syenite
Au deposit
Ag deposit
Pb-Zn deposit
Cu deposit
Fault
124.06°
124.37°
40.22°
40.08°
(c)
0 2km
100# Fault
Heigou Fault
Wulongbei Pluton
Hanjiapu Fault
Wulong Pluton
NWF2
NWF1
Hongshi Fault
Yangjia Fault
Jixingou Fault
Sanguliu Pluton
Zhengjiapuzi Fault
Sidaogou
Quaternary
Liaohe Group Gaixian Formation
Liaohe Group Lieryu Formation
Monzonitic Granite
Pegmatite
Dimica Monzonitic Granite
Biotite Adamellite
Granodiorite
Quartz Diorite
Amphibolite
Gold deposit
Fault

◀Figure 1
a Geological location map of the mining district, **b** simplified geological map of eastern Liaoning, **c** and geological map of the WLGF in eastern Liaoning (modified from Zheng et al., 2022; fault dataset from Gu et al., 2020)

boundary of the WLGF. Additionally, in the eastern part of the WLGF, researchers have speculated the existence of two smaller-scale NW-trending faults with a strike of approximately 320°. These faults dip to the southwest with angles ranging from 50° to 70° (Gu et al., 2020; Zheng et al., 2022).

In the western part of the WLGF, the predominant mineralization type is gold-bearing quartz vein type, while in the east the Sidaogou gold deposit is characterized by the development of both quartz-vein and alteration rock types of gold mineralization (Ji et al., 2009). It should be noted that the gold-bearing quartz veins in the Wulong gold deposit are primarily controlled by secondary-order faults of different directions on both sides of the main NNE-trending fault. However, recent studies have shown that gold mineralization is also developed within some segments of the main NNE-trending fault zone, but with a predominance of alteration rock-type mineralization (Zeng et al., 2019).

3. *Data and Methods*

In this study, we utilized the ambient noise data recorded by the short-period, high-density seismic array (WSP array) deployed by the Institute of Geology and Geophysics, Chinese Academy of Sciences, from May to June in 2019 covering the WLGF of Liaodong (Zheng et al., 2022). The WSP array is equipped with 334 SmartSolo short-period seismometers, the deployment area is 27 km long in the northwest direction and 7 km wide in the north-east direction, and the distance between stations is about 500 m. The station spacing was approximately 500 m, effectively covering most of the faults, rock formations, and gold deposits within the WLGF, including the Hanjiapu Fault (HJP Fault), Hongshi Fault (HS Fault), Yangjia Fault (YF Fault), Jixingou Fault (JXG Fault), Wulongbei Pluton (WLB Pluton), Sangu Pluton (SGL Pluton), and the Wulong gold deposit (Fig. 2).

3.1. *Data Processing*

Many researchers have derived the relationship that the cross-correlation function between two stations is equal to the empirical Green's function (EGF) using theories such as the reciprocity theorem, the stationary phase approximation, and the theory of mode division (Sabra et al., 2005; Wapenaar, 2004; Weaver, 2005). For two stations, A and B, the cross-correlation function can be expressed as follows:

$$C_{AB}(t) = \langle u_A(t) * u_B(-t) \rangle = \int [G_{AB}(-t) - G_{AB}(t)]dt \tag{1}$$

where, $C_{AB}(t)$ represents the cross-correlation function between station A and B, $u_A(t)$ represents the seismic ambient noise signal from station A, $u_B(t)$ represents the seismic record from station B, and G_{AB} represents the Green's function, $\langle\rangle$ and * represent the ensemble average and convolutional computation.

In this study, the EGFs between different stations were obtained by performing cross-correlation calculations (Bensen et al., 2007) on the signals received at each interstation. As an example, the cross-correlation results are shown in WL930 station (Fig. 3).

Based on the obtained cross-correlation functions, this study utilized the Analysis Time Freq method to calculate the dispersion curves of surface waves. The EGF Analysis Time Freq program (Yao et al., 2006) was used for extracting the dispersion curves. Initially, the average of manually picked 1000 dispersion curves was taken as the reference dispersion curve. The dispersion values were assigned within a range of two standard deviations. Only the dispersion curves with a signal-to-noise ratio greater than 5 and interstation distances larger than twice the wavelength were retained (Jiang et al., 2016; Yang et al., 2020). In the end, 54,011 group velocity dispersion curves and 45,435 phase velocity dispersion curves were automatically picked. Despite setting thresholds for dispersion extraction, there were still some issues with the automatically extracted dispersion curves, such as excessively high gradient values or insufficient data points. Therefore, before inversion, quality control was performed on the dispersion data as follows:

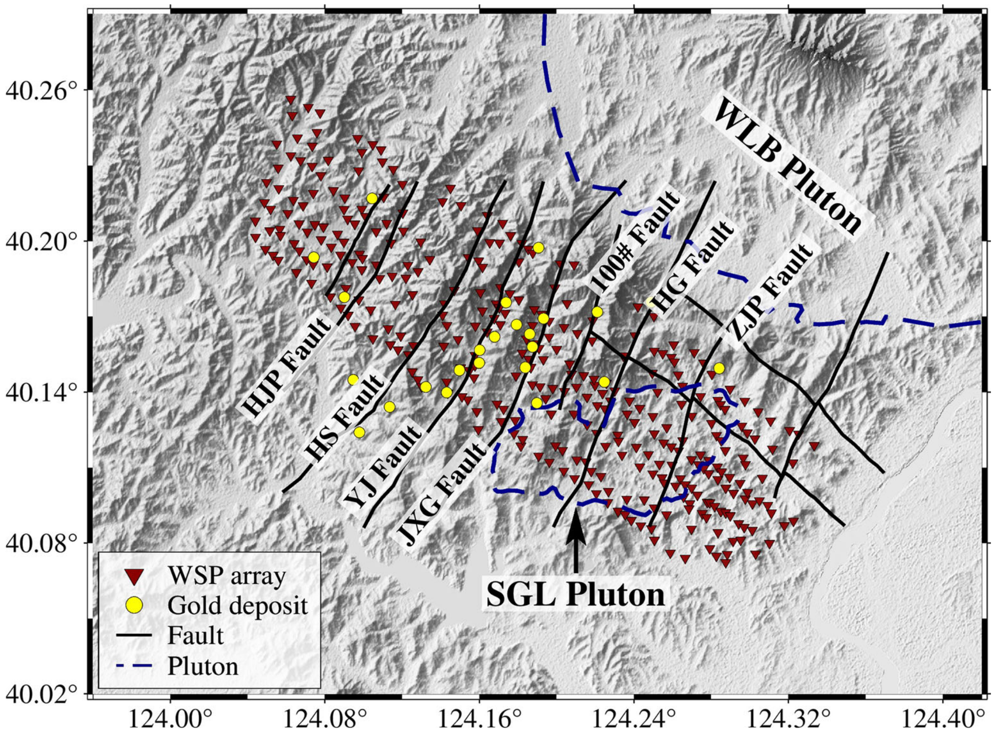

Figure 2
Distribution map of the Wulong Short-Period Dense Array (WSP Array). Red triangles represent short-period seismometers; yellow dots represent gold mining points; black solid lines represent faults. Wulongbei Pluton (WLB Pluton); Sanguliu Pluton (SGL Pluton:); Hanjiapu Fault (HJP Fault); Hongshi Fault (HS Fault); Yangjia Fault (YJ Fault); Jixingou Fault (JXG Fault:); Heigou Fault (HG Fault); Zhengjiapu Fault (ZJP Fault)

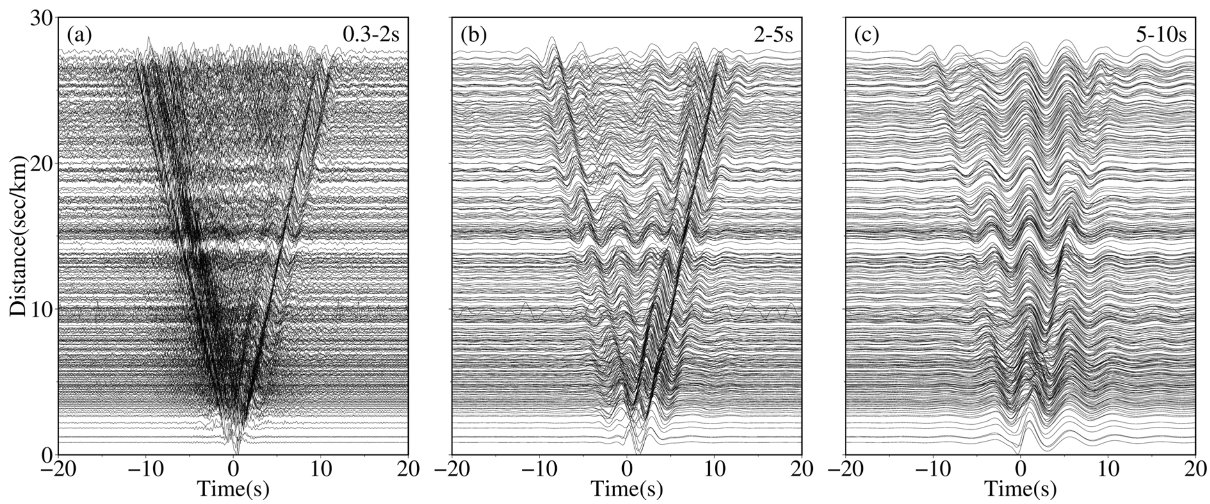

Figure 3
Cross-correlation functions at WL930 station with the other 333 stations. Bandpass-filtered results in different period ranges: **a** 0.3-2s, **b** 2-5s, and **c** 5-10s

(i) Dispersion curves with less than 3 points were removed to reduce accidental variability due to a small number of periods.
(ii) Based on the mean and two standard deviations of all dispersion values, the data outside this range were eliminated. After this procedure, the distribution of residual dispersion curves became more uniform.
(iii) If surface waves propagate along similar paths, their dispersion curves should also be similar (Qiao et al., 2018). Based on this principle, the similarity path method was used to manually identify and remove poorly quality dispersion curves.

After rigorous data quality control, a total of 2962 phase velocity dispersion curves (Fig. 4a) and 9082 group velocity dispersion curves (Fig. 4b) were reserved. The number of ray paths for each period is shown in Fig. 4c. Figures 5a–f display the ray coverage for different periods: the densest ray coverage is observed within the range of 0.3–4s. At a period of 3.4s, the number of ray paths covering the study area is 1053. Although there is relatively limited available dispersion data for periods greater than 3.4 s, the ray coverage within the basin is relatively dense and uniform.

3.2. Inversion Details and Model Resolution Test

In order to obtain the three-dimensional shallow structure of the Goldfield, we conducted a direct inversion method (Fang et al., 2015) using frequency-domain ray tracing and we directly obtain the three-dimensional S-wave velocity beneath the study area from the dispersion curves. For the forward modeling, we used the Fast Marching Method (Rawlinson & Sambridge, 2004), which calculates the ray paths and travel times between the seismic sources and stations. We designed an initial S-wave velocity model based on the empirical relationship proposed by Shearer (2019). To avoid boundary effects, we extended the depth of the initial model to 5.0 km to improve the stability of the inversion (Fig. 6a). The parameterization of the model followed the approach proposed by Boschi & Ekström (2002). In the inversion process, the lateral grid node spacing of the model was set at 0.01° (approximately 1.1 km), and the depth grid node spacing was set at 0.3 km.

In this study, we employed a linearization method to invert S-wave velocity. During the linearization inversion process, each iteration assumes that the current model is relatively close to the real model. We compile the surface wave data from each iteration process into a sparse linear system:

$$\begin{bmatrix} \delta \boldsymbol{t} \\ \mathbf{0} \\ \mathbf{0} \end{bmatrix} = \begin{bmatrix} \mathbf{G} \\ \sigma \boldsymbol{S} \\ \gamma \boldsymbol{I} \end{bmatrix} \delta \boldsymbol{\beta} \tag{2}$$

where, $\mathbf{G}$ represents the data sensitivity kernel. When calculating $\mathbf{G}$ in each iteration, the density and P-wave velocity are both represented by S-wave velocity based on empirical relationships in rock physics (Brocher, 2005). $\delta\boldsymbol{t}$ represents the residuals of dispersion data, $\delta\boldsymbol{\beta}$ represents the update values of S-wave velocity, $\boldsymbol{S}$ represent second order Tikhonov Regulation, σ represents the smoothing parameter, and γ is the damping parameter. We can efficiently solve linear system Eq. (2) by using LSMR algorithm (Fong & Saunders, 2011). We continuously correct the model through multiple iterations, to ensure that the final residuals converge within a reasonable range.

$$\beta_{i+1} = \beta_i + \delta\beta_i \tag{3}$$

where, i is the number of inversion iterations.

During inversion, we used the L-curve method to determine the optimal smoothing coefficient σ. By testing different σ values ranging from 5 to 120, we found that the inflection point occurs at 20, which we selected as the best σ value for our inversion (Fig. 6b).

For model resolution test, the anomaly size is set to $0.04^{\circ} \times 0.04^{\circ} \times 0.9$ km, and the velocity perturbation is disturbance 10% of the background velocity (2.8 km/s). The imaging depth and resolution are constrained by the surface wave period. Considering the effective of group velocity dispersion curves and phase velocity dispersion curves sensitive kernels in this study, it can be concluded that the anomalies is only located within a depth of 3.5 km (Fig. 5g–h). For the horizontal slice, the study area in different depths is well recovered (Fig. 7a–f). For the vertical profile, it is evident that the checkerboard models

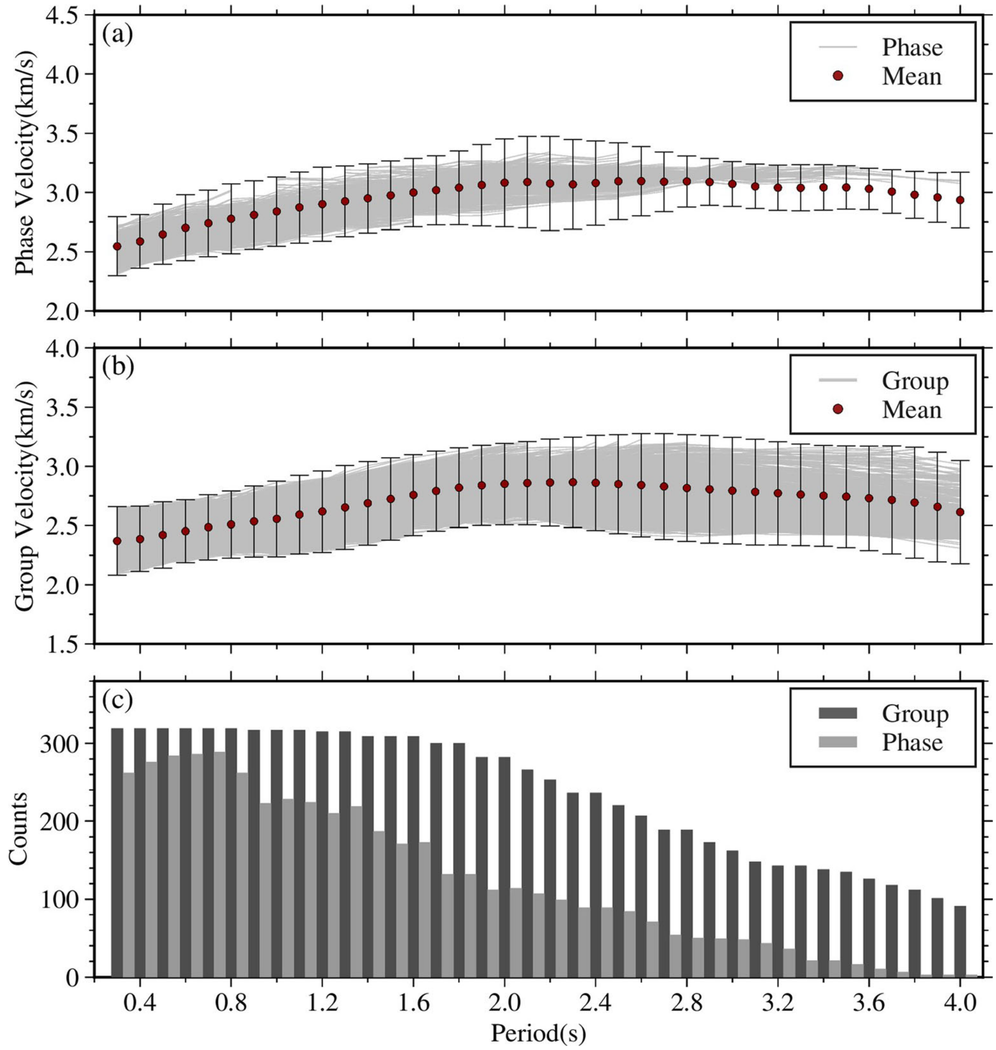

Figure 4
Rayleigh wave dispersion curves. Phase velocity dispersion curves; **b** Group velocity dispersion curve; (red dot represents the mean dispersion curve with standard deviations plotted as error bars) **c** Number of dispersion curves for each period point

exhibit a remarkable recovery within the central portion of the study region (Fig. 7g–j). The entire WLGF demonstrates a successful recovery, with anomalies size 0.040° in the lateral direction and approximately 0.9 km in the vertical direction. This test indicates that the velocity anomalies within the majority of the inversion region can be effectively recovered, thanks to the dense coverage of dispersion curves.

4. Results

Figure 8 shows the inversion results of the S-wave velocity at depths of 0.3 km, 0.6 km, 0.9 km, 1.2 km, 1.5 km, 1.8 km, 2.4 km, 3.0 km, and 3.5 km in the study area. The results indicate the following: In the shallow depth range of 0.3–0.6 km, the S-wave velocity is generally less than 3.0 km/s. There are two intersecting low-velocity zones in the central part of the study area, which are distributed in an NW–SE and NNE-SSW direction, respectively (Fig. 8a–b). Additionally, the S-wave velocity profiles accurately

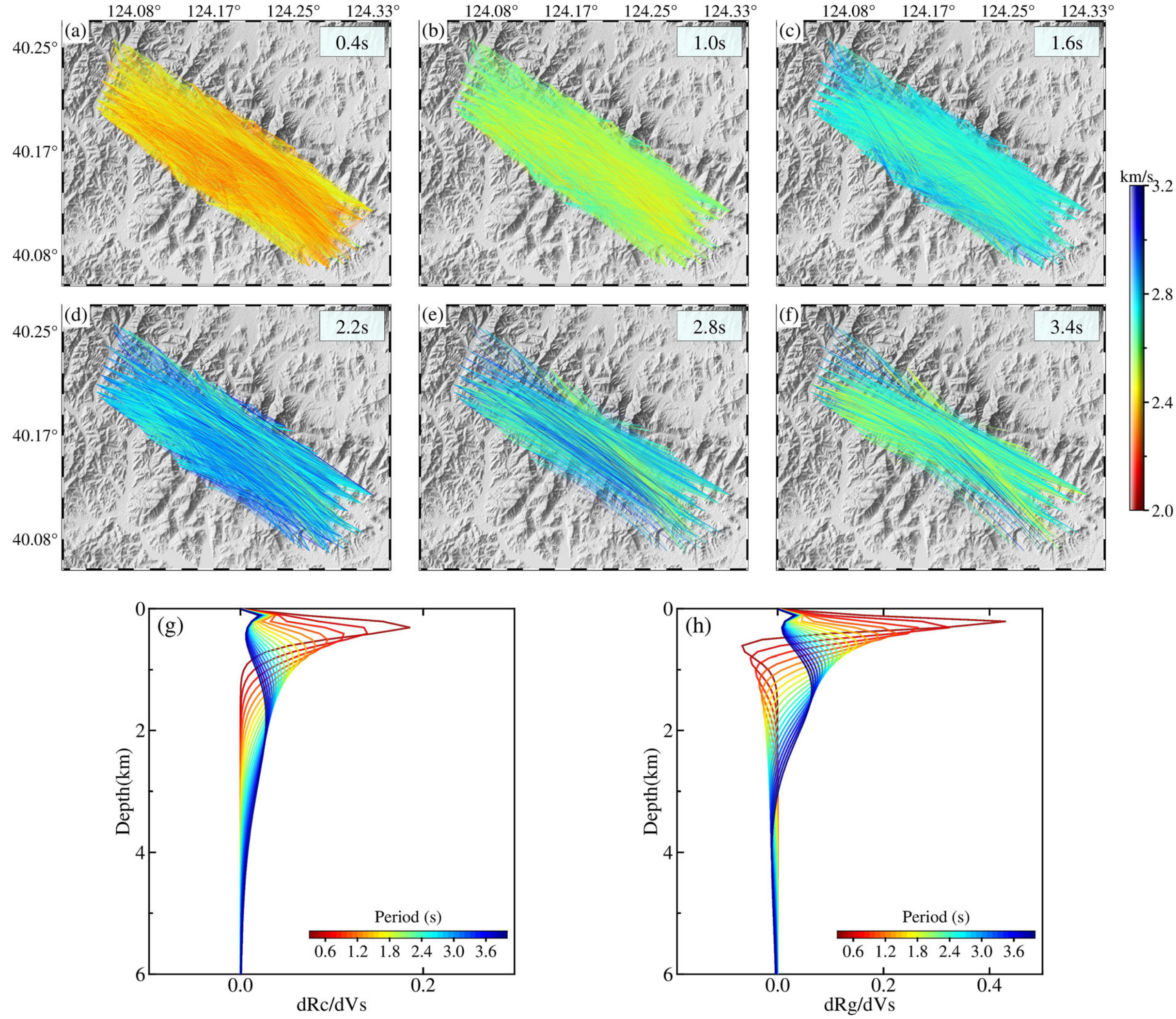

Figure 5
Ray Path Density and Sensitivity Kernel. (**a–f**) Ray path density for different periods. (**g–h**) Rayleigh wave depth sensitivity kernel for different periods

indicate the low-velocity anomalies in the shallow layers. The NW low-velocity zone extends along the profile for a length of about 10 km and persists from the shallow subsurface to a depth of 0.8 km, showing a relatively flat velocity structure within 1 km depth (Fig. 9b–d).

In the depth range of 1.5–3.0 km, the S-wave velocity ranges from 3.0 to 3.5 km/s. There are two distinct high-velocity anomalies located at the northwest and southeast ends of the study area (Fig. 8e–h). The high-velocity anomaly in the northwest extends laterally for about 8 km with a vertical scale of around 2 km. The high-velocity anomaly in the southeast extends laterally for about 13 km with a vertical length of around 1 km. Compared to the high-velocity anomaly in the northwest, the one in the southeast has a flatter planar shape (Fig. 8g, Fig. 9d, Fig. 10). At 3.5 km depth, these two high-velocity anomalies tend to merge and the anomaly intensity decreases relatively (Fig. 8i).

Compared to the velocity structure presented by Zheng (2022), we have observed similar NW and NNE low-velocity anomaly zones at depths shallower than 1.2 km. However, there are two main differences

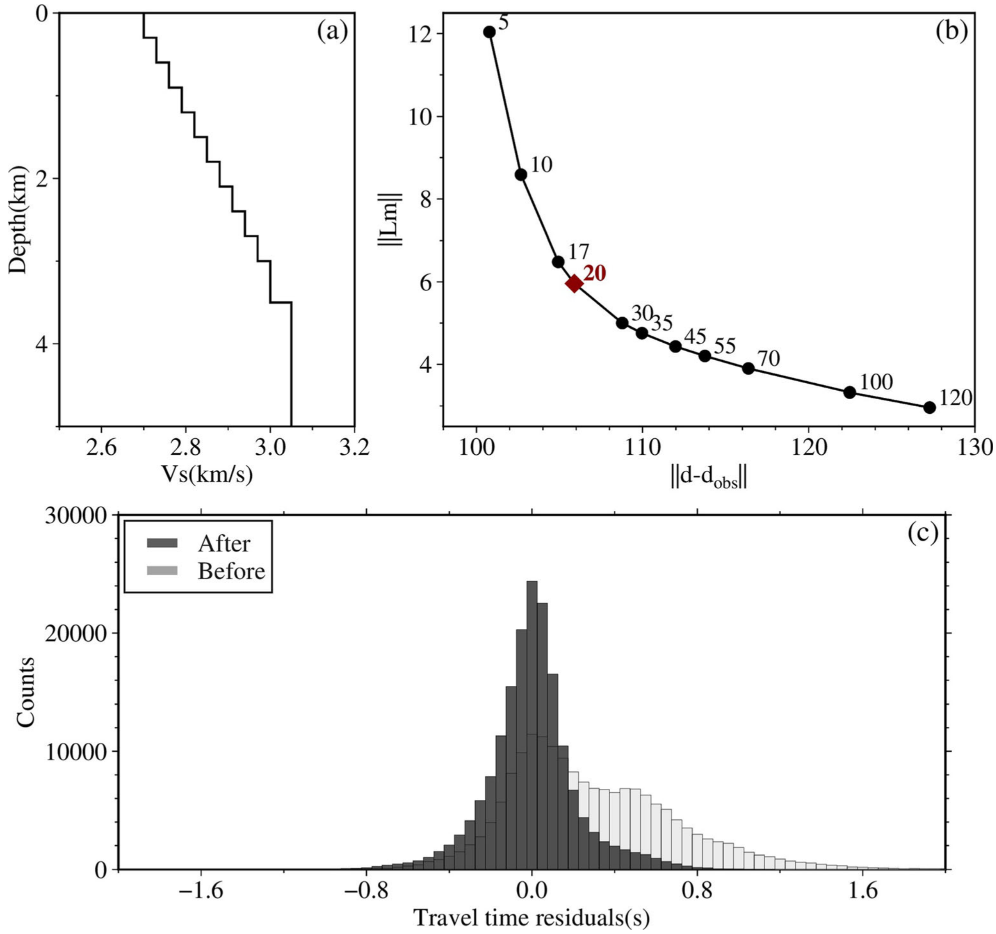

Figure 6

a Initial model for S-wave velocity inversion. **b** L-curve, with red dots indicating the turning point. **c** The histograms of residuals between before and after inversion

between our findings: There are some variations in the low-velocity anomalies in the shallow layers. Due to the inclusion of phase velocity dispersion in the inversion process, the jointly inverted velocity structure extends to greater depths, reaching approximately 3.5 km, and reveals the presence of two high-velocity anomaly. Figure 6c show the travel time residuals before and after inversion. Most of the travel time residuals after inversion significantly reduce to zero, and the residual distribution map is closer to the normal distribution, indicating that our inversion results converge.

5. Discussion

5.1. Geological Interpretation of Velocity Structure in WLGF

It can be observed that the S-wave velocity structure in the WLGF is characterized by three high-velocity anomalies with low-velocity anomaly zones between them (Fig. 8). For convenience, these three high-velocity anomalies are labeled as I, II, & III, and the three low-velocity anomalies are labeled as IV, V & VI in Fig. 8b, g. Based on the geological information of the area, the exposed rocks mainly consist of Middle Jurassic gneissic Wulong granite, Early Cretaceous fine-grained granodiorite/quartz

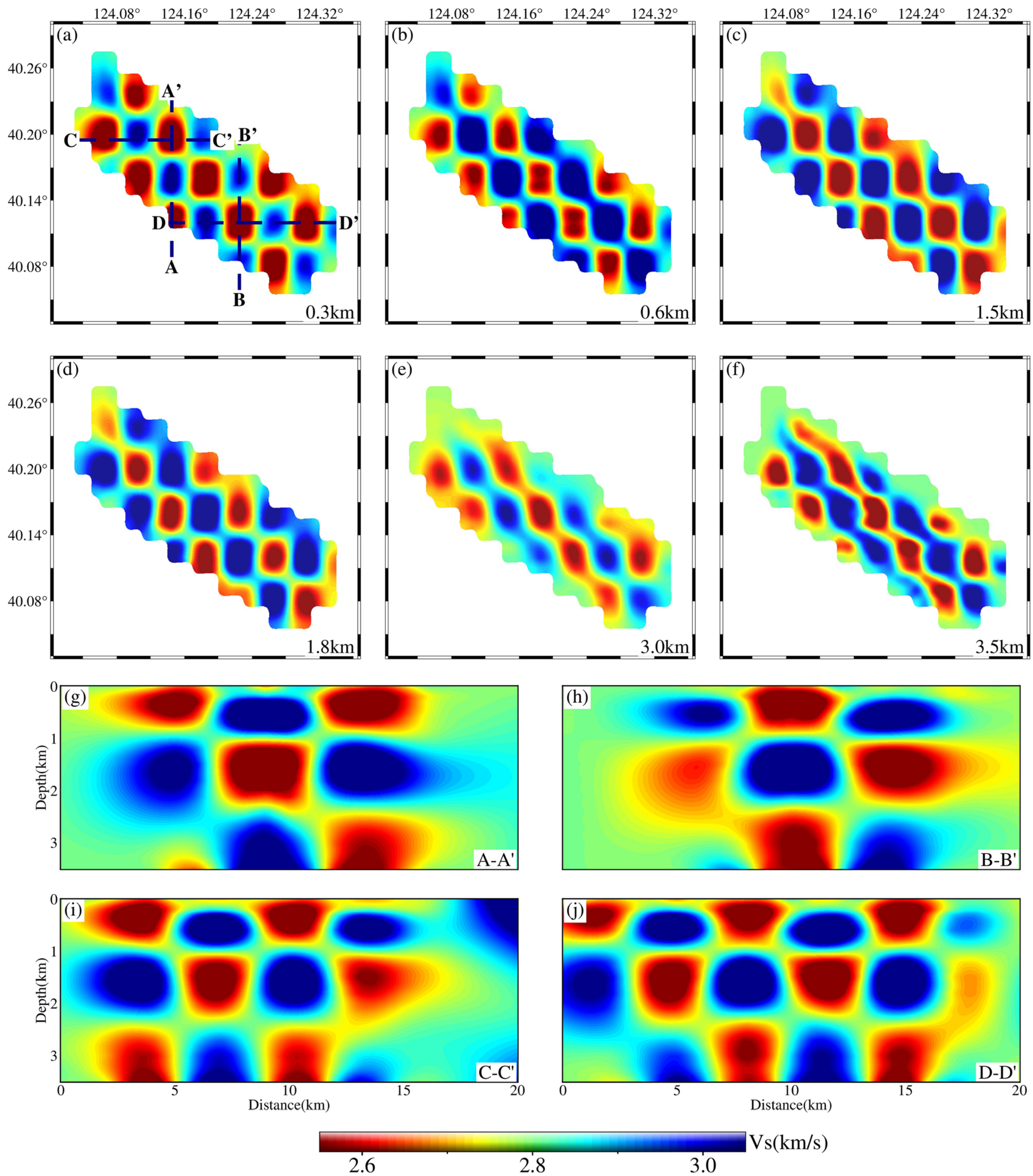

Figure 7
The checkerboard resolution tests. **a** 0.3 km depth, **b** 0.6 km depth, **c** 1.5 km depth, **d** 1.8 km depth, **e** 3.0 km depth, **f** 3.5 km depth, **g** AA' profile, **h** BB' profile, **i** CC' profile, **j** DD' (profile locations show in Fig. 7a)

diorite, and fine grained Granodiorite in Sanguliu. Metamorphic rocks of the Liaohe Group and sandstone of the Diaoyutai Formation are exposed in the southeastern part of the survey area. In the depth slice at 0.3 km below the surface (Fig. 8a), these three high-velocity anomalies are developed in the granite

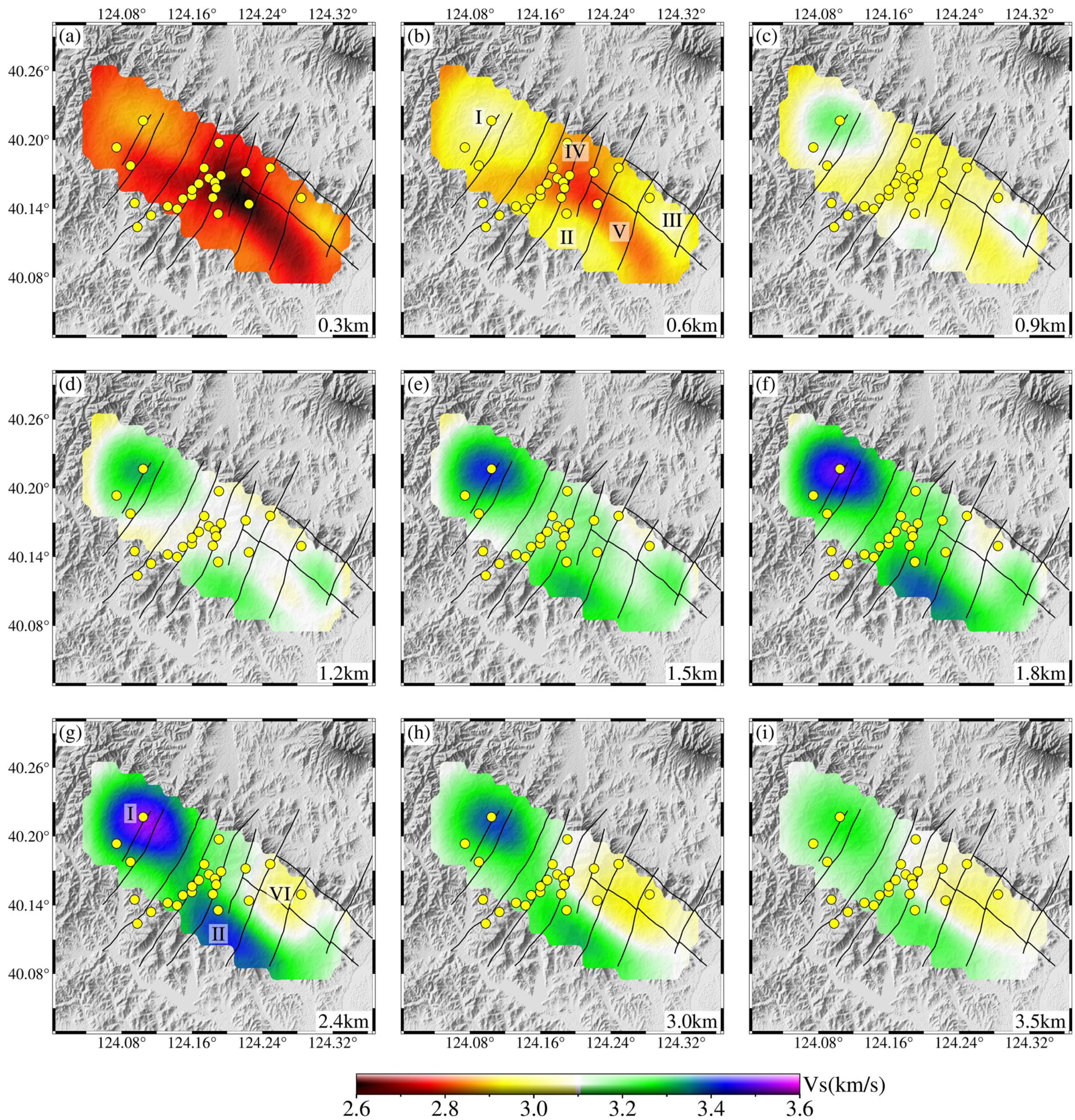

Figure 8

S-wave velocity at different depths in WLGF. **a** 0.3 km depth, **b** 0.6 km depth, **c** 0.9 km depth, **d** 1.2 km depth, **e** 1.5 km depth, **f** 1.8 km depth, **g** 2.4 km depth, **h** 3.0 km depth, **i** 3.5 km depth. (Yellow dots represent gold deposit locations, and black solid lines represent faults)

exposure areas, with anomaly II roughly coinciding with the location of the Sanguliu Pluton. The Liaohu Group and Diaoyutai Formation exhibit weak low-velocity anomalies or background values.

As mentioned earlier, the characteristics of the velocity structure in the study area vary at different depths. In the shallow depth range of 0.3–0.6 km, although the three high-velocity anomalies mentioned above exist, their anomaly strengths are relatively small (around 5.4%), while the low-velocity anomaly zone between them is more prominent (around 6.2%). Overall, it exhibits a crossover of low-velocity

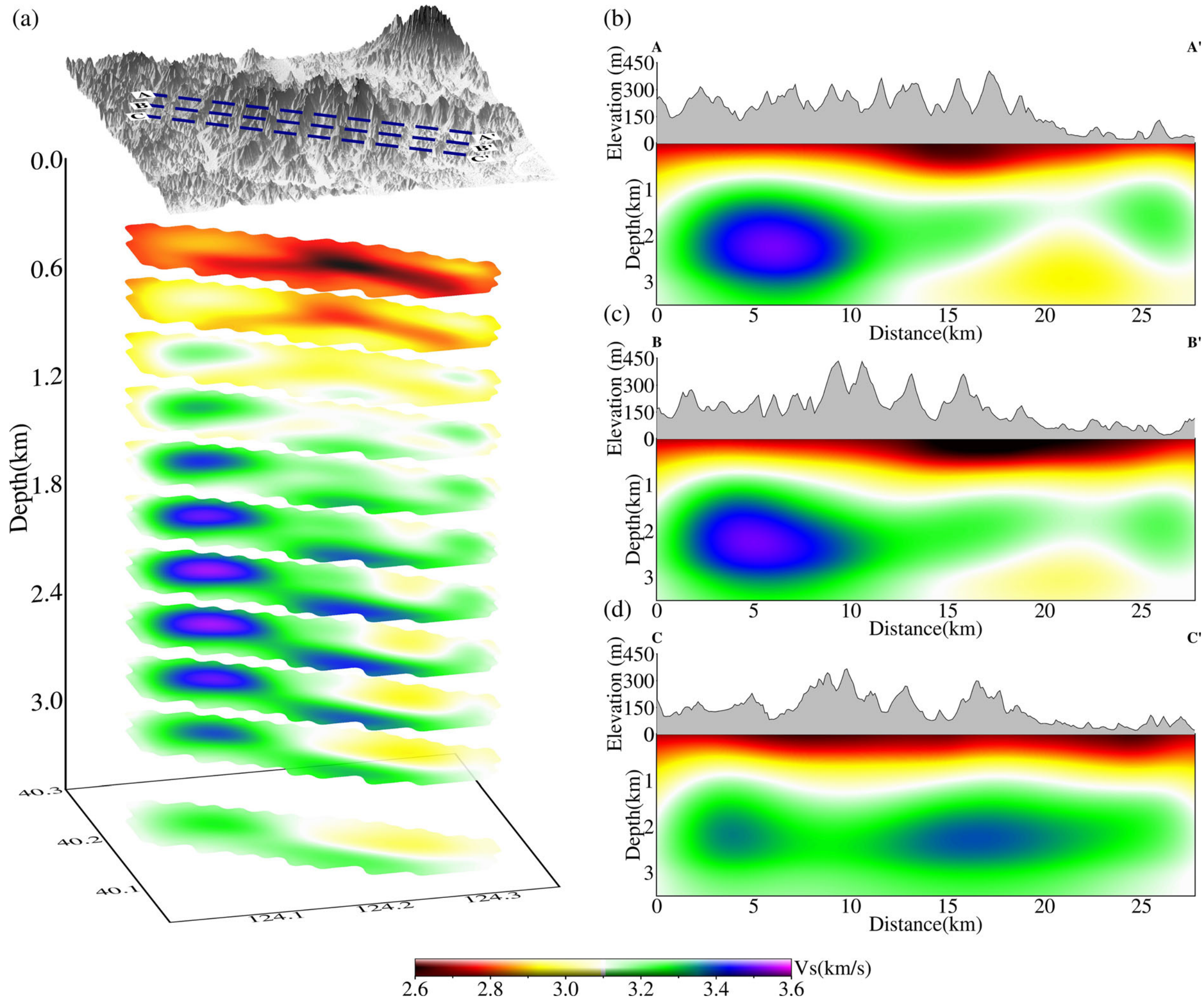

Figure 9
Three-dimensional S-wave velocity structure in WLFG. **a** Spatial distribution map of S-wave velocity structure at different depths. **b**–**d** S-wave velocity structure beneath profile AA', BB', and CC' (profile locations show in Fig. 9a)

anomaly zones in the NNE and NW directions. The anomaly IV is consistent with the orientation of NNE-oriented faults in the area, while the anomaly V is approximately parallel to the previously inferred NW fault (Fig. 8a–c).

Based on the geological and velocity structure characteristics mentioned above, we interpret the low-velocity anomaly in the survey area as the result of hydrothermal alteration along fault zones or contact zones between intrusive bodies and surrounding rocks. It needs noted that the NW anomaly V does not align perfectly with the previously inferred NW fault direction (Fig. 8a–b), and there is a slight variation in its orientation in the eastern and western segments. This weak inconsistency may be influenced by two factors: first, there may be some deviation in the previously inferred fault orientation because no NW-oriented faults are observed on the 1:200,000 or 1:50,000 geological maps; second, if the inferred NW fault does indeed exist, dip angle may vary significantly in the vertical direction. Because the fault traces on different depth slices represent the vertical projection of the fault trace on the surface rather than the actual position of the fault. Regardless of the reasons for this difference, we believe that this significant low-velocity anomaly zone is likely the

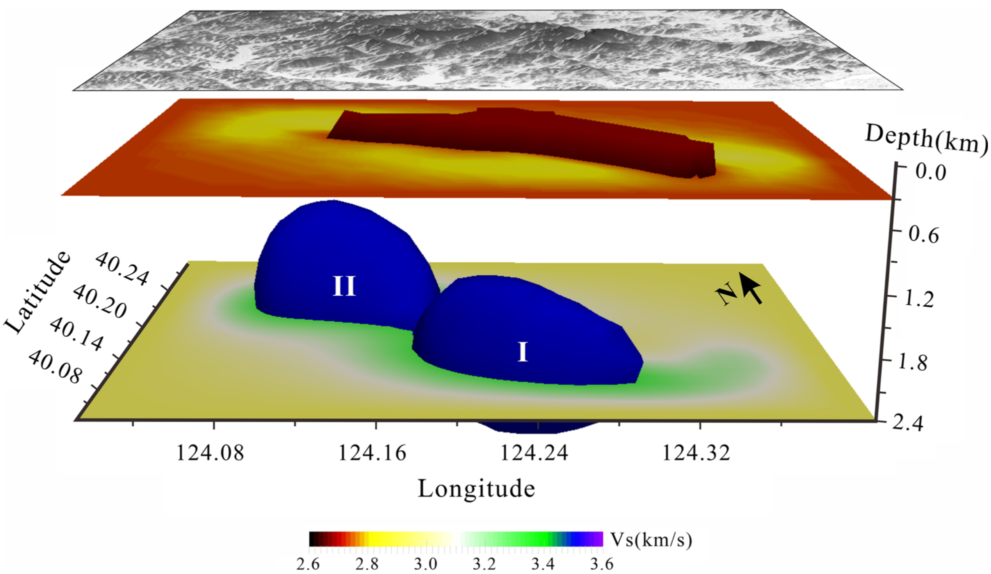

Figure 10
Three-dimensional S-wave velocity structure in WLGF

result of hydrothermal activity along the mineralizing fault system, indicating that the intersection of the anomaly IV and anomaly V may represent the most important hydrothermal activity center in the WLGF. This interpretation is supported by the fact that the largest Wulong gold deposit and a series of medium- and small-sized deposits are spatially distributed within and near this low-velocity anomaly zone (Fig. 8). On the other hand, in the western segment of the anomaly V, no-fault structures have been observed on the surface. Therefore, the presence of this low-velocity anomaly in that area may suggest the existence of a concealed NW-oriented fault.

In the depth range of 1.5–3.0 km, the velocity structure in the survey area is characterized by the more prominent presence of the three high-velocity anomalies mentioned earlier, especially anomaly I (around 14.5% anomaly strength). At the same time, anomalies II and III merge and connect each other between 1.5–2.4 km. Overall, the Middle Jurassic gneissic granite (such as the Wulong Pluton, previously considered as Paleoproterozoic migmatitic granite) and the metamorphic sequences of the Liaohe Group exhibit low-velocity characteristics, while the Early Cretaceous fine-grained quartz monzodiorite-granodiorite-tonalite (such as the Sanguliu Pluton) exhibit high-velocity anomalies. This is consistent with the composition and structural characteristics of these two types of rocks or plutons. Therefore, we speculate that high-velocity anomaly I may represent a concealed pluton with similar compositions and ages to the Sanguliu Pluton. Based on the scale of the velocity anomalies (Fig. 9a, Fig. 10), this concealed pluton may not be smaller than the Sanguliu Pluton and may extend to a greater depth.

5.2. *Implications for Deep Exploration Potential in WLGF*

Petrological and ore deposit studies have shown that the gold deposits in the WLGF were formed in the Early Cretaceous (130–120 Ma) and are genetically related to the Early Cretaceous magmatism represented by the Sanguliu Pluton (Yu et al., 2020). Therefore, the presence of a concealed pluton in the northwest part of the WLGF, which may have similar compositions and ages to the Sanguliu Pluton, is of significant geological and exploration importance, as this concealed pluton likely provided at least some ore-forming fluids and materials. Based on the spatial distribution of the discovered deposits (occurrences) within the WLGF, they are mainly located in the low-velocity anomaly zone between the concealed pluton and the Sanguliu Pluton. These low-velocity anomaly zones are the result of hydrothermal alteration processes associated with the circulation and migration of ore-forming fluids along fault zones or contact zones between plutons (with possible superimposed faulting). On the other hand, the velocity structure in this study reveals that the Sanguliu Pluton and the concealed pluton may be connected and merged into a larger intrusive body between 2.4 and 3.0 km depth. Therefore, theoretically, there is mineralization potential within this depth range and adjacent areas between the two plutons.

Currently, there is no definitive data available regarding the deep extension of the controlling fault system in the WLGF. Firstly, for the NW-oriented faults that are not manifested at the surface and shallow levels, they appear to be more prominent in the deep layers. For example, between the depth range of 2.4–3.5 km, the boundary between the high-velocity anomaly II represented by the Sanguliu Pluton and the large low-velocity anomaly VI to the north appears to be straight and exhibits clear characteristics of a fault structure (Fig. 8g–i). This suggests that the NW-oriented faults, as a rock-controlling structure, may control the emplacement of the Sanguliu Pluton. Secondly, the NNE-oriented faults are distributed in a nearly equidistant pattern (3–6 km) at the surface and extend along the trend for at least 20 km. Therefore, they should easily cut through the concealed basement, indicating that these faults function as ore-controlling structures within the mineralization system of the WLGF. Furthermore, in the case of the largest gold deposit in the area, the Wulong gold deposit, although the main mineralized structures are the secondary faults with various directions alongside the NNE-oriented main fault, alteration-type mineralization within the NNE-oriented main fault zone has been identified (Zeng et al., 2019). These observations suggest that there is a high potential to explore alteration-type gold mineralization in the NNE-oriented fault zones between the Sanguliu Pluton and the concealed pluton that is between the Sanguliu Pluton and concealed pluton.

The characteristics of gold mineralization in the WLGF of Liaodong, where quartz vein-type mineralization occurs alongside the main faults and alteration-type gold mineralization develops in the deeper parts of the main faults, bear a striking resemblance to the Zhaoyuan-Laizhou gold belt in the Jiaodong Peninsula. In the Zhaoyuan-Laizhou gold belt, large-scale alteration-type gold mineralization is prevalent within the main fault zones (such as the Jiaojia-Xincheng Fault, Zhaoyuan-Pingdu Fault, and Fushan Fault), while quartz vein-type mineralization dominates in the secondary fault zones on either side (such as the Shangzhuang gold deposit, Caojiawa gold deposit, and Linglong gold deposit). Given the proximity of Jiaodong and Liaodong in terms of regional tectonic setting and their spatial relationship across the Bohai Bay, the similarities in the style of ore-controlling faults and gold mineralization characteristics suggest extensive exploration potential in the deeper part of the WLGF. Considering the results of the velocity structure obtained in this study, we believe that the area between the Sanguliu Pluton and the concealed pluton in the northwest, along the NNE-oriented main fault, particularly at the intersection of the NNE and NW-oriented fault zones, holds the potential for the formation of large to giant alteration-type gold deposits, making it the most promising exploration target.

6. *Conclusions*

(1) Within 1.2 km of the shallow crust in the WLGF in Liaodong, the S-wave velocity structure is characterized by significant low-velocity anomalies in the NNE and NW directions (anomalies IV & V), while in the deeper parts (between 1.5 and 2.4 km), two high-velocity anomalies I & II are observed.

(2) Among the two high-velocity anomalies in the deeper part, the anomaly II aligns with the surface-exposed Sanguliu Pluton, while the other (anomaly I) is interpreted as a concealed pluton with similar compositions and ages as the Sanguliu Pluton. The cross-point of the NNE- and NW-trending low-velocity anomalies (IV & V) in the shallow part is the result of hydrothermal alteration associated with ore-forming fluid

circulation along the ore-controlling fault systems, indicating that this intersection is likely the center of hydrothermal activity in the area.

(3) Based on the characteristics of gold deposits in the WLGF, it is proposed that the region between the Sanguliu Pluton and the concealed pluton (I) in the northwest holds favorable conditions for mineralization, particularly in the deeper parts at the intersection of the NNE- and NW-trending faults (low-velocity anomalies IV & V), indicating a good prospect for exploring gold resource (alteration-type).

Acknowledgements

We would like to express our gratitude for the great efforts of the Liaoning Oilfield Geophysical Corporation of China Petroleum Eastern Geophysical Company during the data acquisition process for the WSP array. We also extend our appreciation to the Seismic Array Laboratory at the Institute of Geology and Geophysics, Chinese Academy of Sciences, and the Department of Earth and Space Sciences at the Southern University of Science and Technology for their strong support. Thanks to Researcher Tianyu Zheng, Professor Wei Zhang, Guangbing Hou, Qilin Tu, Zhiming Bai, Youshan Liu, Yuan Ling, Jincheng Xu, Minfu Huang, Weiyu Dong, Yuepeng Huang, Long Li, Yang He, and others for their assistance and support during the fieldwork. This work was supported by the National Nature Sciences Foundation of China (42130807, 42104102) and National Key Research and Development Program of China (2016YFC0600101).

Author contribution All authors contributed to the study conception and design. Material preparation, data collection and analysis were performed by Tingwei Yang, Tao Xu and Fan Zheng. The first draft of the manuscript was written by Tingwei Yang and all authors commented on previous versions of the manuscript. All authors read and approved the final manuscript.

Funding

National Nature Sciences Foundation of China, 42130807, National Key Research and Development Program of China, 2016YFC0600101

Data availability

Data used in this study is available upon request from the corresponding author.

Declarations

Conflict of interest The authors declare no competing interests.

References

Bensen, G., Ritzwoller, M., Barmin, M., Levshin, A. L., Lin, F., Moschetti, M., Shapiro, N., & Yang, Y. (2007). Processing seismic ambient noise data to obtain reliable broad-band surface wave dispersion measurements. *Geophysical Journal International, 169*, 1239–1260. https://doi.org/10.1111/j.1365-246X.2007.03374.x

Boschi, L., & Ekström, G. (2002). New images of the Earth's upper mantle from measurements of surface wave phase velocity anomalies. *Journal of Geophysical Research: Solid Earth, 107*(B4), ESE1–ESE12. https://doi.org/10.1029/2000JB000059

Brocher, T. M. (2005). Empirical relations between elastic wavespeeds and density in the Earth's crust. *Bulletin of the Seismological Society of America, 95*(6), 2081–2092. https://doi.org/10.1785/0120050077

Deng, J., Yang, L. Q., Groves, D. I., Zhang, L., Qiu, K. F., & Wang, Q. F. (2020). An integrated mineral system model for the gold deposits of the giant Jiaodong province, eastern China. *Earth Science Reviews, 208*, 103274. https://doi.org/10.1016/j.earscirev.2020.103274

Dong, W., Xu, T., Ai, Y., Fan, E., Li, L., & Hou, J. (2022). The boundary between the North China Craton and the Central Asian Orogenic Belt in NE China: Seismic evidence from receiver function imaging. *Journal of Asian Earth Sciences*, *237*, 105360. https://doi.org/10.1016/j.jseaes.2022.105360

Duan, X. X., Zeng, Q. D., Yang, J. H., Liu, J. M., Wang, Y. B., & Zhou, L. L. (2014). Geochronology, geochemistry and Hf isotope of Late Triassic magmatic rocks of Qingchengzi district in Liaodong peninsula. *Northeast China. Journal Asian Earth Science, 91*, 107–124. https://doi.org/10.1080/00206814.2020.1852448

Fan, X., Chen, Q. F., Ai, Y., Chen, L., Jiang, M., Wu, Q., & Guo, Z. (2021). Quaternary sodic and potassic intraplate volcanism in northeast China controlled by the underlying heterogeneous lithospheric structures. *Geology, 49*, 1260–1264.

Fang, H. J., Yao, H. J., Zhang, H. J., Huang, Y. C., & Van der Hilst, R. D. (2015). Direct inversion of surface wave dispersion for three-dimensional shallow crustal structure based on ray tracing: Methodology and application. *Geophysical Journal International, 201*, 1251–1263. https://doi.org/10.1093/gji/ggv080

Feng, H. X., Shen, P., Zhu, R. X., Li, C. H., Ma, G., & Pan, H. D. (2019). Geology and He-Ar-S-Pb isotope constraints on the genesis of the Sidaogou gold deposit in Liaodong Peninsula, northeastern North China Craton. *Ore Geology Reviews, 113*, 103080. https://doi.org/10.1016/j.oregeorev.2019.103080

Feng, H. X., Shen, P., Zhu, R. X., Ma, G., Li, C. H., & Li, J. P. (2020). SIMS U-Pb dating of vein-hosted hydrothermal rutile and carbon isotope of fluids in the Wulong lode gold deposit, NE China: Linking gold mineralization with craton destruction. *Ore Geology Reviews, 127*, 103838. https://doi.org/10.1016/j.oregeorev.2020.103838

Fong, D. C. L., & Saunders, M. (2011). LSMR: An iterative algorithm for sparse least-squares problems. *SIAM Journal on Scientific Computing, 33*(5), 2950–2971. https://doi.org/10.1137/10079687X

Gu, Y. C., Chen, R. Y., Li, D. T., Yang, J. L., Yang, F. C., Jia, H. X., Dick, J., Hu, Q. H., Ju, N., & Cao, J. (2018). Jurassic ca. 160 Ma crustal remelting and Paleoproterozoic intrusive rock residues in the Liaodong Peninsula, East China: Evidence from in situ zircon U-Pb dating and Lu–Hf isotopic analysis. *Geological Journal, 53*, 174–188. https://doi.org/10.1002/gj.3206

Gu, Y. C., Zhao, Y., Yang, Z. Z., Zhang, P., Yang, F. C., Ju, N., Xu, J., Yang, H. Z., Bi, Z. W., & Wei, Y. M. (2020). Zircon U-Pb ages, elements geochemistry and Sr-Nd-Pb-Hf Isotopic characteristics of Wulong remelting granite intrusive rocks in Liaodong Peninsula and geological significance (in Chinese with English abstract). *Earth Science—Journal of China University of Geosciences, 45*, 3913–3933. https://doi.org/10.3799/dqkx.2020.220

Ji, Z. J., Wu, X. G., & Huang, J. P. (2009). Study on structure-controlling regularities of mineralization and geological criteria for prospecting in Wulong gold deposit (in Chinese with English abstract). *Gold, 30*(07), 19–22. https://doi.org/10.3969/j.issn.1001-1277.2009.07.005

Jiang, C., Yang, Y., & Zheng, Y. (2016). Crustal structure in the junction of Qinling Orogen, Yangtze Craton and Tibetan Plateau: Implications for the formation of the Dabashan Orocline and the growth of Tibetan Plateau. *Geophysical Journal International, 205*, 1670–1681. https://doi.org/10.1093/gji/ggw096

Li, Z., Chen, B., Liu, J. W., Zhang, L., Yang, C., & Chuan, Y. (2015). Zircon U-Pb ages and their implications for the South Liaohe Group in the Liaodong Peninsula, Northeast China (in Chinese with English abstract). *Acta Petrologica Sinica, 31*(6), 1589–1605.

Li, J., Cai, W. Y., Wang, K. Y., Kim, N., Liu, H. L., Lee, G. J., & Yoo, B. C. (2020). Initial decratonization of the eastern North China Craton: New constraints from geochronology, geochemistry, and Hf isotopic compositions of Mesozoic igneous rocks in the Qingchengzi district. *Geological Journal, 55*, 3796–3820. https://doi.org/10.1002/gj.3635

Liu, D. Y., Nutman, A. P., Compston, W., Wu, J. S., & Shen, Q. H. (1992). Remnants of $\geq$ 3800 Ma crust in the Chinese part of the Sino-Korean craton. *Geology, 20*, 339–342. https://doi.org/10.1130/0091-7613(1992)020%3c0339:ROMCIT%3e2.3.CO;2

Liu, J. M., Zhao, G. C., Xu, G., Sha, D. M., Xiao, C. H., Fang, X., Liu, F. X., Guo, Q., & Yu, H. (2020). Structural control and genesis of gold deposits in the liaodong peninsula, northeastern north china craton. *Ore Geology Reviews, 125*, 103672. https://doi.org/10.1016/j.oregeorev.2020.103672

Luo, Y., Sun, M., Zhao, G. C., Li, S. Z., Xu, P., Ye, K., & Xia, X. P. (2004). LA-ICP-MS U-Pb zircon ages of the Liaohe Group in the Eastern Block of the North China Craton: Constraints on the evolution of the Jiao-Liao-Ji Belt. *Precambrian Research, 134*, 349–371. https://doi.org/10.1016/j.precamres.2004.07.002

Ma, L., Xu, T., Ai, Y., Yang, J., Yang, Y., Fan, E., Li, L., Hou, J., & Dong, W. (2022). Hot lithosphere beneath the northeastern North China Craton detected by ambient noise tomography. *Tectonophysics*, *839*, 229551. https://doi.org/10.1016/j.tecto.2022.229551

Miao, L. C., Qiu, Y. M., Fan, W. M., Zhang, F. Q., & Zhai, M. G. (2005). Geology, geochronology, and tectonic setting of the Jiapigou gold deposits, southern Jilin Province. *China. Ore Geology Reviews, 26*, 137–165. https://doi.org/10.1016/j.oregeorev.2004.10.004

Qiao, L., Yao, H., Lai, Y. C., Huang, B. S., & Zhang, P. (2018). Crustal structure of Southwest China and Northern Vietnam from ambient noise tomography: Implication for the large-scale material transport model in SE Tibet. *Tectonics, 37*, 1492–1506. https://doi.org/10.1029/2018TC004957

Rawlinson, N., & Sambridge, M. (2004). Wave front evolution in strongly heterogeneous layered media using the fast marching method. *Geophysical Journal International, 156*, 631–647. https://doi.org/10.1016/j.oregeorev.2020.103672

Sabra, K. G., Gerstoft, P., Roux, P., Kuperman, W., & Fehler, M. C. (2005). Extracting time-domain Green's function estimates from ambient seismic noise. *Geophysical Research Letters, 32*, L03310. https://doi.org/10.1029/2004GL021862

Shearer, P. M. (2019). *Introduction to Seismology*. Cambridge University Press.

Wang, Y., Yu, B., Zeng, Q., Guo, W., Yang, J., & Meng, Q. (2019). Petrogenesis and tectonic setting of the Wulong two-mica monzogranite on Liaodong Peninsula, NE China: Constraints from zircon U-Pb and Hf-O isotopic data. *Geochemical Journal, 53*, 261–279. https://doi.org/10.2343/geochemj.2.0564

Wang, Z. Q., Huhua, Z. F., Chen, B., Duan, X. X., Zhou, T. F., & Jiang, X. (2020). The petrogenesis of the Early Cretaceous Sanguliu pluton in the Liaodong Peninsula, NE China: Constrained from the trace-element modelling and Sr-Nd isotopes (in Chinese with English abstract). *Acta Petrologica Sinica, 36*(12), 3683–3704. https://doi.org/10.18654/1000-0569/2020.12.08

Wapenaar, K. (2004). Retrieving the elastodynamic Green's function of an arbitrary inhomogeneous medium by cross correlation. *Physical Review Letters, 93*, 254301. https://doi.org/10.1103/PhysRevLett.93.254301

Weaver, R. L. (2005). Information from seismic noise. *Science, 307*, 1568–1569. https://doi.org/10.1126/science.1109834

Wu, F. Y., Yang, J. H., Wilde, S. A., & Zhang, X. O. (2005). Geochronology, petrogenesis and tectonic implications of Jurassic granites in the Liaodong Peninsula, NE China. *Chemical Geology, 221*, 127–156. https://doi.org/10.1016/j.chemgeo.2005.04.010

Xie, T., Xu, T., Ai, Y., Zeng, Q., Zhang, W., & Zheng, F. (2021). Imaging the shallow crustal velocity structure of the Qingchengzi ore field on the Liaodong Peninsula, China, with a short-period dense array using ambient noise tomography. *Tectonophysics*, *813*, 228913. https://doi.org/10.1016/j.tecto.2021.228913

Xu, T., Ai, Y., Wu, C., Chen, L., Fan, E., Li, L., & Dong, W. (2023). Subduction-induced asthenospheric flow around the Songliao Basin in NE China revealed by Shear Wave splitting measurements of dense seismic arrays. *Journal of Geophysical Research: Solid Earth*, *128*(3), e2022JB026075. https://doi.org/10.1029/2022JB026075

Xu, X. B., Zhao, L., Wang, K., & Yang, J. F. (2018). Indication from finite-frequency tomography beneath the North China Craton: The heterogeneity of craton destruction. *Science China Earth Sciences, 61*, 1238–1260. https://doi.org/10.1007/s11430-017-9201-y

Yang, T., Xu, T., Ai, Y., Yang, J., & Yuan, H. (2024). Fine crust-mantle structure of the major tectonic boundaries between the North China Craton and Central Asian Orogenic Belt revealed from Rayleigh wave phase velocities and receiver functions. *Journal of Geophysical Research: Solid Earth*, *129*(7), e2024JB028857. https://doi.org/10.1029/2024JB028857

Yang, Y., Yao, H., Wu, H., Zhang, P., & Wang, M. (2020). A new crustal shear-velocity model in Southwest China from joint seismological inversion and its implications for regional crustal dynamics. *Geophysical Journal International, 220*, 1379–1393. https://doi.org/10.1093/gji/ggz514

Yao, H., Hilst, R., & Hoop, M. (2006). Surface-wave array tomography in SE Tibet from ambient seismic noise and two-station analysis—I Phase Velocity Maps. *Geophysical Journal International, 166*, 732–744. https://doi.org/10.1111/j.1365-246X.2006.03028.x

Yu, B., Zeng, Q. D., Frimmel, H. E., Wang, Y. B., Guo, W. K., Sun, G. T., Zhou, T. C., & Li, J. P. (2018). Genesis of the Wulong gold deposit, northeastern North China Craton: Constraints from fluid inclusions, HOS-Pb isotopes, and pyrite trace element concentrations. *Ore Geology Reviews, 102*, 313–337. https://doi.org/10.1016/j.oregeorev.2018.09.016

Yu, B., Zeng, Q. D., Frimmel, H. E., Qiu, H. C., Li, Q. L., Yang, J. H., Wang, Y. B., Zhou, L. L., Chen, P. W., & Li, J. P. (2020). The 127 Ma gold mineralization in the Wulong deposit, Liaodong Peninsula, China: Constraints from molybdenite re-Os, monazite U-Th-Pb, and zircon U-Pb geochronology. *Ore Geology Reviews, 121*, 103542. https://doi.org/10.1016/j.oregeorev.2020.103542

Zeng, Q. D., Chen, R. Y., Yang, J. H., Sun, G. T., Yu, B., Wang, Y. B., & Chen, P. W. (2019). The metallogenic characteristics and exploring ore potential of the gold deposits in eastern Liaoning Province (in Chinese with English abstract). *Acta Petrologica Sinica, 35*(7), 1939–1963.

Zhai, M. G., Yang, J. H., Fan, H. R., Miao, L. C., & Li, Y. G. (2002). A large-scale cluster of gold deposits and metallogenesis in the eastern North China Craton. *International Geology Review, 44*, 458–476. https://doi.org/10.2747/0020-6814.44.5.458

Zhang, P., Zhao, Y., Chai, P., Yang, H. Z., & Na, F. C. (2017). Geochemistry, Zircon U-Pb analysis, and biotite 40Ar/39Ar geochronology of the Maoling gold deposit, Liaodong rift NE China. *Resource Geology, 67*, 426–441. https://doi.org/10.1111/rge.12133

Zhang, Z. Q., Wang, G. W., Carranza, E. J., Zhang, J. J., Tao, G. S., Zeng, Q. D., Sha, D. M., Li, D. T., Shen, J. F., & Pang, Z. (2019). Metallogenic model of the Wulong gold district, China, and associated assessment of exploration criteria based on multi-scale geoscience datasets. *Ore Geology Reviews, 114*, 103138. https://doi.org/10.1016/j.oregeorev.2019.103138

Zhang, S., Zhu, G., Xiao, S. Y., Su, N., Liu, C., Wu, X. D., Yin, H., Li, Y. J., & Lu, Y. C. (2020). Temporal variations in the dynamic evolution of an overriding plate: Evidence from the Wulong area in the eastern North China Craton China. *Geological Society of American Bulletin, 132*, 2023–2042. https://doi.org/10.1130/B35465.1

Zheng, F., Xu, T., Ai, Y., Yang, Y., Zeng, Q., Yu, B., & Xie, T. (2022). Metallogenic potential of the Wulong goldfield, Liaodong Peninsula, China revealed by high-resolution ambient noise tomography. *Ore Geology Reviews, 142*, 104704. https://doi.org/10.1016/j.oregeorev.2022.104704

Zheng, F., Xu, T., Ai, Y., Ge, Y., Zeng, Q., Miao, L., Dong, W., & Badal, J. (2024). Deep structure of the Wulong goldfield, Liaodong Peninsula, China, revealed by receiver functions: Implications for the tectonic and mineralization dynamics. *Frontiers in Earth Science*, *12*, 1437605. https://doi.org/10.3389/feart.2024.1437605

Zhu, R., & Sun, W. (2021). The big mantle wedge and decratonic gold deposits. *Science China Earth Sciences, 64*(9), 1451–1462. https://doi.org/10.1007/s11430-020-9733-1

Zhu, R. X., Fan, H. R., Li, J. W., Meng, Q. R., Li, S. R., & Zeng, Q. D. (2015). Decratonic gold deposits. *Science China: Earth Sciences, 58*, 1523–1537. https://doi.org/10.1007/s11430-015-5139-x

Zhu, R., Yang, J. H., Wang, G., Zeng, Q., Xue, G., Xu, T., Li, X., Zhang, P., Lei, D., & Zhu, G. (2024). The genesis and resource potential of gold deposits in the Liaodong Peninsula. *Science China Earth Sciences*, *67*(3), 657–672. https://doi.org/10.1007/s11430-023-1258-4

(Received July 25, 2023, revised December 13, 2023, accepted August 7, 2024, Published online August 28, 2024)